Gradient-elasticity for honeycomb materials: validation and identification from full-field measurements

Julien Réthoré, Christine Kaltenbrunner, Thi Bach Tuyet Dang, Philippe Chaudet, Manuel Kuhn

Gradient-elasticity for honeycomb materials: validation and identification from full-field measurements

Julien Réthoré, Christine Kaltenbrunner, Thi Bach Tuyet Dang, Philippe Chaudet

LaMCoS, Université de Lyon / INSA Lyon / CNRS UMR 5259
Bat. Jacquard, 27 Avenue Jean Capelle, F-69621 Villeurbanne, Cedex, France

Manuel Kuhn

Mechanical Engineering Department, INSA Lyon
Bat. Jacquard, 27 Avenue Jean Capelle, F-69621 Villeurbanne, Cedex, France

Abstract

Gradient-elasticity and more generally gradient-enhanced continuum models have been extensively developed since the beginning of the twentieth century. These models have shown the ability to account for the effect of the underlying material heterogeneity at the macroscopic scale of the continuum. Despite of a great theoretical interest, gradient-enhanced models are usually difficult to interpret physically and even more to identify experimentally. This paper proposes an attempt to validate and identify from experimental data, a gradient-elasticity model for a material with a periodic microstructure . A set of dedicated experimental and numerical tools are developed for this purpose: first, the design of an experiment, then two-scale displacement field measurements by digital image correlation with dedicated post-processing techniques and finally a model updating technique. This paper ends up with the full set of first and second-order elastic constants of a gradient-elastic model which macroscopic kinematic has been validated by investigating the deformation of the unit cells at the microscopic scale.

Keywords: gradient-elasticity, digital image correlation, identification

Email address: julien.rethore@insa-lyon.fr (Julien Réthoré)

1. Introduction

Gradient-elasticity and more generally gradient-enhanced continuum models have been extensively developed since the pioneering work by Cosserat et al. (1909); Mindlin (1964); Toupin (1964) and Eringen and Suhubi (1964). These models have shown a number of useful properties for *e*.g. capturing size effects. The main purpose of these models is to incorporate the effect of the underlying heterogeneity of materials at the macroscopic scale of the continuum. Despite of a great theoretical interest, gradient-enhanced models are usually not easy to interpret physically. They are also difficult to implement numerically because they lead to higher order partial differential equations that require higher continuity of the displacement description. Furthermore, these models involve numerous material constants, the full set of these constants being almost impossible to obtain experimentally. Among the reasons for the gradient-enhanced material parameters to be difficult to identify experimentally, is their localized influence (where intense strain variations occur) and the low amplitude of their contribution to the global response of a material. To circumvent these experimental difficulties, a great effort has been made by researchers to develop accurate homogenization techniques of higher order. Among the proposed methodologies, one could mention the work by Kouznetsova et al. (2002); Forest (1998) or Gologanu et al. (1995). However, as evidenced by Forest and Trinh (2011), the hypothesis of these homogenization techniques concerning the deformation of the control volume is not clear and the estimation of effective properties of a heterogeneous material is therefore subjected to some limitations.

The recent development of full-field displacement measurement techniques by digital image correlation allowing for a strong coupling between experiments and numerical simulations, *e*.g. Besnard et al. (2006); Réthoré et al. (2008, 2013), opens new per-

spectives for studying experimentally gradient-enhanced models. Indeed, they allow for a local investigation of the kinematic field during the experiment and, there is thus a potential for validating and/or identifying the material constants of gradient-enhanced models. In Burteau et al. (2012), an attempt to measure the deformation of a cellular material at the cells' scale was proposed. However, the deformation parameters are estimated from the analysis of the morphology of the cells before and after deformation, without quantifying the local deformation of the material at the microscopic scale.. Using full-field measurements, this paper proposes a first attempt to validate and identify a gradient-elasticity model for a material with a periodic micro-structure. A set of dedicated experimental and numerical tools are developed for this purpose. First, the design of an experiment allowing for activating gradient-related phenomena in a model material is presented in Section 2. Then, in Section 3, the validation of a strain-based micro-morphic kinematic is proposed using the displacement fields measured at both the scale of the material micro-structure and the scale of the analyzed structure. Last, Section 4 is dedicated to the identification of the macroscopic continuum derived from the experimentally validated micro-macro kinematic relationship.

2. Experimental setup

2.1. Sample

To investigate experimentally the variations of the displacement in a heterogeneous media at different scales, a special setup has been designed. This setup is based on a specimen loaded in tension. The loading device is standard but the specimen is obtained from a 3D printer. As shown in Figure 1, it has a central squared shaped part with an honeycomb structure (periodic tilling of hexagonal unit cells) whereas the ends of the sample are made homogeneous in order to be clenched by the grips. The global coordinate frame $(\underline{\mathbf{e}}_1, \underline{\mathbf{e}}_2)$ is defined in Figure 1 as the horizontal and vertical

axis. The honeycomb cell's edge is 0.68 mm and the cell wall thickness is 0.29 mm. The overall dimension of the central part of the specimen is 90 mm. Its thickness is 10 mm. The honeycomb structure is thus made of 67×67 cells. A row of 15 cells with an angle of 30^o, with respect to the loading direction ($\underline{\mathbf{e}}_1$), has been removed in the center of the specimen to create a strongly varying multi-axial strain state.

2.2. Digital Image Correlation

A black and white speckle pattern has been applied on the specimen surface using spraid paint. During the test, a digital camera records images of the specimen surface with a definition of 6576×4384 pixels to allow for displacement field measurements using digital image correlation. The camera is mounted with a 200 mm lens leading to a conversion factor from pixel to meter of 19 μm per pixel. Using this setup, the distance between two unit cell centers along the horizontal axis is 66 pixels. Digital image correlation is based on the local conservation of the grey levels between two images f and g:

$$f(\underline{\mathbf{X}}_p) = g(\underline{\mathbf{X}}_p + \underline{\mathbf{d}}(\underline{\mathbf{X}}_p)), \tag{1}$$

$\underline{\mathbf{X}}_p$ giving the position of a pixel in the global coordinate system and $\underline{\mathbf{d}}$ being the unknown measured displacement. A non-linear least-squares resolution scheme of this equation is adopted in the following (Besnard et al., 2006). This allows for using, as in the following, a finite element mesh to define the unknown kinematic. Minor modifications in the implementation of the technique compared to what was proposed by Besnard et al. (2006) have been adopted. Mainly, the image gradient is calculated using a central finite difference scheme and the sub-pixel grey level interpolation is cubic-spline. Here, the reference image f, shown in Figure 1, is recorded with zero force and g is the image recorded just before specimen failure.

Using this setup, first, the local and global variations of the measured displacement

field are analyzed in Section 3. Then, the effective properties of the macroscopic continuum are identified in Section 4.2.

3. Two-scale displacement field analysis

3.1. Theoretical background

The displacement field of a heterogeneous media is usually considered at two separate scales. From a material point at the macroscopic scale defined by its coordinates $\underline{\mathbf{X}}$, a local microscopic volume is described through the local coordinates $\underline{\mathbf{x}} = \varepsilon\underline{\mathbf{X}}$. This change of scale is defined by the small parameter ε set as the ratio between the characteristic size of the control volume l and the characteristic size of the macro-scale L. In this context, the local fluctuations of the displacement at the microscopic scale $\underline{\mathbf{u}}(\underline{\mathbf{X}}, \underline{\mathbf{x}})$ are expanded around a given material point X:

$$\underline{\mathbf{u}}(\underline{\mathbf{X}}, \underline{\mathbf{x}}) = \underline{\mathbf{u}}_0(\underline{\mathbf{X}}, \underline{\mathbf{x}}) + \varepsilon\underline{\mathbf{u}}_1(\underline{\mathbf{X}}, \underline{\mathbf{x}}) + \varepsilon^2\underline{\mathbf{u}}_2(\underline{\mathbf{X}}, \underline{\mathbf{x}}) + \cdots . \tag{2}$$

Equation (2) is then transformed following Boutin (1996) to set the local displacement $\underline{\mathbf{u}}$ as a combination of local boundary value problems depending on the macroscopic kinematic variables $\underline{\mathbf{U}}(\underline{\mathbf{X}})$ and its gradients:

$$\underline{\mathbf{u}}(\underline{\mathbf{X}}, \underline{\mathbf{x}}) = \underline{\mathbf{U}}(\underline{\mathbf{X}}) + \varepsilon\underline{\mathbf{L}}_1(\underline{\mathbf{x}}, \underline{\nabla}_{\underline{\mathbf{X}}}\underline{\mathbf{U}}(\underline{\mathbf{X}})) + \varepsilon^2\underline{\mathbf{L}}_2(\underline{\mathbf{x}}, \underline{\nabla}_{\underline{\mathbf{X}}}\underline{\nabla}_{\underline{\mathbf{X}}}\underline{\mathbf{U}}(\underline{\mathbf{X}})) + \cdots , \tag{3}$$

where $\underline{\mathbf{L}}_1, \underline{\mathbf{L}}_2$ are localization operators to be defined. These boundary value problems classically use the macroscopic kinematic variables to prescribe the local displacement fluctuations on the boundary of the control volume. As the expansion in Equation (2) has been limited, intentionally, to order 2, a quadratic polynomial (Gologanu et al., 1995; Forest, 1998, *e*.g.) is subsequently used to prescribe the variation

$$\underline{\tilde{\mathbf{u}}}(\underline{\mathbf{x}}) = \underset{\sim}{\mathbf{F}}.(\underline{\mathbf{x}} - \underline{\mathbf{X}}) + \frac{1}{2}\underset{\simeq}{\mathbf{D}} : ((\underline{\mathbf{x}} - \underline{\mathbf{X}}) \otimes (\underline{\mathbf{x}} - \underline{\mathbf{X}})) \tag{4}$$

of $\underline{\mathbf{u}}$ on the boundary of the control volume $V(\underline{\mathbf{X}})$. In this definition, $\underset{\sim}{\mathbf{F}}$, respectively $\underset{\simeq}{\mathbf{D}}$, are kinematic parameters of the deformation of the unit cell. The operators . and : define simple and double contraction and $\otimes$ the tensorial product. In practice, Dirichlet boundary conditions as defined by $\underline{\tilde{\mathbf{u}}}$ reveal too stiff when estimating the effective properties of the heterogeneous media. Further, in the case of a material obtained by a periodic tilling of unit cells, a supplementary fluctuation $\underline{\mathbf{v}}$ is allowed:

$$\left(\underline{\mathbf{u}}(\underline{\mathbf{X}},\underline{\mathbf{x}}) - \underline{\mathbf{U}}(\underline{\mathbf{X}})\right)_{\partial V(\underline{\mathbf{X}})} = \underline{\tilde{\mathbf{u}}}(\underline{\mathbf{x}}) + \underline{\mathbf{v}}(\underline{\mathbf{x}}). \tag{5}$$

This additional fluctuation is usually assumed to have a periodic behaviour but it has been shown by Forest and Trinh (2011) that a non-periodic fluctuation may be obtained in practice. This results were obtained by analyzing full-field finite element simulations. The aim of this section is to investigate these conditions experimentally.

3.2. Displacement fields

Two analyses are performed. The first is aimed at measuring the macroscopic displacement ($\underline{\mathbf{d}} \equiv \underline{\mathbf{U}}$ in Equation (1)) using the mesh defined in Figure 2(a). Each node of this mesh corresponds to a vertex of the periodic tilling used to generate the honeycomb structure. In other words, each node corresponds to the center of a unit cell. The second analysis is aimed at evaluating the kinematic of each individual unit cell ($\underline{\mathbf{d}} \equiv \underline{\mathbf{u}}$) of the central part of the specimen. For this purpose, the mesh for one unit cell as presented by Figure 2(b) is duplicated using the same periodic tilling as for generating the honeycomb.

The result of the first analysis is presented in Figure 3(a). As expected, the macroscopic displacement $\underline{\mathbf{U}}$ is discontinuous across the notch in the center of the honeycomb structure. The amplitude of this displacement (about 30 pixels) is such that the signal over noise ratio is about 500, the displacement thus appears extremely smooth.

This has been made possible thanks to the high definition camera used in the experiment. For comparison purposes, the microscopic displacement fluctuation $\underline{\mathbf{u}}$ is presented in Figure 3(b). A good qualitative agreement is obtained between the two analyses. A deeper analysis of the unit cells' kinematic is performed below to assess the relationship between the displacement measured at the macro scale and the one measured at the micro scale.

3.3. Microscopic fluctuations analysis

From the displacement field presented in Figure 3(b), the displacement of the boundary of each unit cell is extracted. First, its mean value is computed and compared to $\underline{\mathbf{U}}$ in Figure 3(c). A very good agreement is obtained concerning this zero-order term of the expansion in Equation (3). This result states as an experimental validation of the zero-order micro-macro kinematic relation:

$$\underline{\mathbf{U}}(\underline{\mathbf{X}}) = \langle \underline{\mathbf{u}}(\underline{\mathbf{x}}) \rangle_{V(\underline{\mathbf{X}})} = \frac{1}{V} \int_{V(\underline{\mathbf{X}})} \underline{\mathbf{u}}((\underline{\mathbf{X}}, \underline{\mathbf{x}}) \mathrm{d}V. \tag{6}$$

The remaining effective displacement $\underline{\mathbf{u}}(\underline{\mathbf{X}}, \underline{\mathbf{x}}) - \underline{\mathbf{U}}(\underline{\mathbf{X}})$ is now projected in a least-squares sense onto the quadratic polynomial $\underline{\tilde{\mathbf{u}}}$ defined by Equation (4). Due to the existence of an additional fluctuation $\underline{\mathbf{v}}$ that is supposed to be periodic, the projection is not performed along the entire boundary of the unit cells. It is preferred to project the difference between the effective displacement $\underline{\mathbf{u}}(\underline{\mathbf{X}}, \underline{\mathbf{x}}) - \underline{\mathbf{U}}(\underline{\mathbf{X}})$ of pairs of homologous points along half of the unit cells' boundary. This allows for eliminating the additional periodic fluctuation from the analysis. Let us denote $\underline{\mathbf{w}}$ the periodic part of the additional fluctuation $\underline{\mathbf{v}}$. The residual of the projection gives access to the remaining non-periodic fluctuation $\underline{\mathbf{v}} - \underline{\mathbf{w}}$. The norm (Euclidean norm of the vector containing the values of $\underline{\mathbf{v}} - \underline{\mathbf{w}}$ along the unit cells' boundary) of this residual is plotted in Figure 4(b). This Figure assesses for the relevance of second order kinematic assumption for the boundary of the unit cells. This assessment is emphasized when the

results are compared to those obtained using a projection onto a first order kinematic (considering vanishing $\underset{\sim}{\mathbf{D}}$) as presented in Figure 4(a). The improvement due to second order is difficult to observe directly from residual maps. However, it is evidenced that the first order give rise to higer residual in the vicinity of the *crack* tip and in a lesser extent along the left and the right edges of the analyzed zone. A quantitative comparison of the residual obtained for the first or the second order polynomial leads to a decrease of: the average projection residual from 10% to 9%, the maximum residual from 65% to 44%. To further illustrate these differences, Figure 5 shows, for the unit cell at the upper *crack* tip, the comparison of the projection of $\underline{\tilde{\mathbf{u}}}$ and the additional fluctuation $\underline{\mathbf{v}}$ for the first and second order scheme. On the upper plots 5(a), 5(b), it is shown that, due to the additional fluctuation $\underline{\mathbf{v}}$, the projected boundary displacement $\underline{\tilde{\mathbf{u}}}$ is slightly different from the actual effective displacement $\underline{\mathbf{u}} - \underline{\mathbf{U}}$ and also slightly different between first and second order. The bottom plots show the additional fluctuation $\underline{\mathbf{v}}$ and its periodic part $\underline{\mathbf{w}}$ for the two projections. It is observed that for the first order compared to the second order, not only the amplitude of $\underline{\mathbf{v}}$ is higer but also the amplitude of the residual $\underline{\mathbf{v}} - \underline{\mathbf{w}}$.

From this analysis, the conclusion arises that a second order kinematics is required for describing the effective displacement at the microscopic scale. For a complete definition of the deformation of the honeycomb material, the comparison of the macroscopic displacement gradient and the micro-morphic $\underset{\sim}{\mathbf{F}}$ is performed. The first component F_{11} of $\underset{\sim}{\mathbf{F}}$ corresponding to the gradient along $\underline{\mathbf{e}}_1$ of the displacement along $\underline{\mathbf{e}}_1$ is compared in Figure 6 to the same component of the gradient of the measured macroscopic displacement $U_{1,1}$. To evaluate the gap between the macroscopic strain $U_{1,1}$ in Figure 6(a) and the microscopic tensor component F_{11} in Figure 6(b), the relative strain is plotted in Figure 6(c). Except at the close vicinity of the *crack* tips, the relative strain is very low (below 0.001 compared to strain level of about 0.01). The

higher values concentrated at the tips of the *crack* are difficult to interpert because the macroscopic strain $U_{1,1}$ is a piecewise constant element field that is transfered to nodes to be compared to F_{11}. This transfert leads to an unavoidable loss of information. The relative strain value remaining to about one tenth of the macroscopic strain, higher relative strain values migh be considered as not meaningful. Drawn with the appropriate precaution, the conclusion arises that the micro-morphic tensor $\underset{\sim}{\mathbf{F}}$ matches the macroscopic displacement gradient. This means that the macroscopic continuum can be considered as a micro-morphic medium with the macroscopic displacement gradient as micro-morphic tensor, or equivalently as a second order continuum. In this context, the first-order micro-macro kinematic relation

$$\underline{\nabla}_{\underline{\mathbf{X}}}\,\underline{\mathbf{U}}(\underline{\mathbf{X}}) = \langle \underline{\nabla}_{\underline{\mathbf{x}}}\,\underline{\mathbf{u}}(\underline{\mathbf{x}})\rangle_{V(\underline{\mathbf{X}})} = \frac{1}{V}\int_{V(\underline{\mathbf{X}})} \underline{\nabla}_{\underline{\mathbf{x}}}\,\underline{\mathbf{u}}((\underline{\mathbf{X}},\underline{\mathbf{x}})\mathrm{d}V \tag{7}$$

is validated.

Based on the results obtained in this Section, it is evidenced that the micro-scale displacement fluctuation follows a polynomial form (plus additional periodic fluctuations) of order 2 at least. The analysis of the relative strain leads to the assumption of second order macroscopic continuum. The kinematic relationships, of order 0 and 1, between the macro-scale displacement and the micro-scale displacement fluctuation due to the heterogeneity of the material have also been validated experimentally .

4. Gradient-elasticity

4.1. Macroscopic continuum

To fulfill the requirements established from the two-scale analysis of the displacement, the modeling of the macroscopic continuum describing the behaviour of the honeycomb material must incorporate strain gradient as a kinematic variable. Within

the framework proposed by Mindlin (1964), $\underset{\sim}{\mathbf{E}}$, the symmetric gradient of the displacement $\underline{\mathbf{U}}$, and $\underset{\approx}{\boldsymbol{\kappa}}$, the gradient of $\underset{\sim}{\mathbf{E}}$, are chosen as the descriptors of the kinematic of the continuum:

$$\underset{\sim}{\mathbf{E}} = \frac{1}{2}(\underline{\nabla}_{\underline{\mathbf{X}}}\,\underline{\mathbf{U}} + \underline{\nabla}^{T}_{\underline{\mathbf{X}}}\,\underline{\mathbf{U}}) \qquad\qquad \underset{\approx}{\boldsymbol{\kappa}} = \underline{\nabla}_{\underline{\mathbf{X}}}\,\underset{\sim}{\mathbf{E}}. \tag{8}$$

Using index notation, this is rewritten as

$$E_{ij} = \frac{1}{2}(U_{i,j} + U_{j,i}) \qquad\qquad \kappa_{ijk} = E_{ij,k} = \frac{1}{2}(U_{i,jk} + U_{j,ik}). \tag{9}$$

The strain energy density Ψ subsequently depends on these two kinematic variables, $\Psi = \Psi(\underset{\sim}{\mathbf{E}}, \underset{\approx}{\boldsymbol{\kappa}})$. The classical Cauchy stress and the hyper-stress are then defined as

$$\underset{\sim}{\boldsymbol{\Sigma}} = \frac{\partial \Psi}{\partial \underset{\sim}{\mathbf{E}}} \qquad\qquad \underset{\approx}{\mathbf{S}} = \frac{\partial \Psi}{\partial \underset{\approx}{\boldsymbol{\kappa}}}. \tag{10}$$

Under the assumption that there is no coupling between first and second order term, the following expression for Ψ is obtained:

$$\Psi(\underset{\sim}{\mathbf{E}}, \underset{\approx}{\boldsymbol{\kappa}}) = \underset{\sim}{\mathbf{E}} : \underset{\sim}{\boldsymbol{\Sigma}} + \underset{\approx}{\boldsymbol{\kappa}} \vdots \underset{\approx}{\mathbf{S}}. \tag{11}$$

The behaviour of such a continuum thus relies on two constitutive linear operators. The first order elastic tensor $\underset{\approx\approx}{\mathbf{C}}$ which establishes the linear relationship between stress and strain reads

$$\underset{\sim}{\boldsymbol{\Sigma}} = \underset{\approx\approx}{\mathbf{C}} : \underset{\sim}{\mathbf{E}}, \qquad i.e. \qquad \Sigma_{ij} = C_{ijkl} E_{kl}, \tag{12}$$

and the second order elastic tensor $\underset{\approx\approx\approx}{\mathbf{A}}$ which plays the same role for the hyper-stress and the strain gradient:

$$\underset{\approx}{\mathbf{S}} = \underset{\approx\approx\approx}{\mathbf{A}} \vdots \underset{\approx}{\boldsymbol{\kappa}}, \qquad i.e. \qquad S_{ijk} = A_{ijklmn} \kappa_{lmn}. \tag{13}$$

In 2D, due to symmetry considerations, the number of material constants in $\underset{\approx\approx}{\mathbf{C}}$ reduces to 6 in the fully anisotropic case. In this context, for $\underset{\approx\approx\approx}{\mathbf{A}}$, the maximum number of material constants is 21. However, the material analyzed in this paper has the properties

of a material symmetry of class D_6: it is invariant by rotation of $\frac{2\pi}{6}$ plus invariant by translation along the tilling directions. This induces a physical symmetry for the elastic operators $\underset{\approx}{\mathbf{C}}$ and $\underset{\approx\approx}{\mathbf{A}}$. Following Auffray et al. (2009), the physical symmetry class for $\underset{\approx}{\mathbf{C}}$ is isotropic which reduces the number of material constants to 2. The physical symmetry of $\underset{\approx\approx}{\mathbf{A}}$ is not isotropic and it requires 5 constants (instead of 4 in isotropic case). In matrix vector format, Equation (13) is written as

$$\begin{bmatrix} S_{111} \\ S_{112} \\ S_{121} \\ S_{122} \\ S_{221} \\ S_{222} \end{bmatrix} = \begin{bmatrix} b_{11} & 0 & 0 & \frac{b_{11}-b_{33}-\sqrt{2}b_{35}}{2} & b_{13} & 0 \\ & b_{33}+b_{22}-b_{11} & b_{22}-b_{11}+\frac{b_{35}}{\sqrt{2}} & 0 & 0 & b_{11}-b_{22}+b_{13} \\ & & b_{33}-3b_{11}-2b_{13}+4b_{22} & 0 & 0 & 3b_{11}-b_{33}-2b_{22}-\sqrt{2}b_{35} \\ & & & b_{11}+b_{33}-2b_{13} & b_{35} & 0 \\ & & Sym & & b_{33} & 0 \\ & & & & & b_{22} \end{bmatrix} \begin{bmatrix} \kappa_{111} \\ \kappa_{112} \\ \kappa_{121} \\ \kappa_{122} \\ \kappa_{221} \\ \kappa_{222} \end{bmatrix}, \tag{14}$$

where $b_{11}, b_{22}, b_{33}, b_{13}$ and b_{35} are the 5 second order intrinsic elastic constants. The lower triangular part of $\underset{\approx\approx}{\mathbf{A}}$ is obtained by symmetry. It has been omitted for conciseness.

4.2. *Identification strategy*

The identification of the material parameters of $\underset{\approx}{\mathbf{C}}$ and $\underset{\approx\approx}{\mathbf{A}}$ is performed by using a Finite Element Model Updating (FEMU) strategy. The basic principle of this technique is to compare the result of a finite element simulation with the experimental data and then to update the parameters of the finite element model in order to minimize the gap between numerical and experimental data (Kavanagh and Clough, 1971). In the context of full-field measurements by digital image correlation performed using a finite element description of the displacement fields, the method is made straightforward (Réthoré, 2010). FEMU consists of a least squares minimization with respect to the material parameters (denoted in a generic format as a vector Λ) of the gap between the measured displacement field and the simulated displacement field:

$$\Lambda_{opt} = \mathrm{Arg}\min_{\Lambda} \frac{1}{mes(\Omega)} \int_{\Omega} \| \underline{\mathbf{U}}_{DIC} - \underline{\mathbf{U}}_{FE}(\Lambda) \|^2 \mathrm{d}\Omega. \tag{15}$$

In this equation, Λ_{opt} is the set of identified parameters and Ω is the surface covered by the finite element mesh used for both the digital image correlation and the

finite element simulations. Note that the measured displacement is used directly as the prescribed displacement along the mesh boundary submitted to Dirichlet's boundary conditions. FEMU strategies have been the subject of significant improvements in the past few years, especially concerning the robustness of the identified parameters to noise measurements (Leclerc et al., 2009; Réthoré, 2010). For the analysis of the data presented in this paper, the noise affecting the measured displacement is of very low amplitude. A standard FEMU procedure is thus used in the sequel.

In the previous section, the left and right edges of the honeycomb zone were identified as pushing the second order kinematic to its limits. These zones are thus omitted for the identification of the gradient-elasticity constitutive operators. A triangular mesh, with elements being independent on the underlying unit cells, fitting a zone of reduced width and describing the *crack* is adopted. This mesh, presented in Figure 7 together with the measured displacement field has an element size of 110 pixels with mesh refinement to 45 pixels in the vicinity of the *crack*. Gradient-elasticity simulations are performed using the C^1 triangular elements proposed by Dasgupta and Sengupta (1990). The use of C^1 shape functions allows for establishing a primal weak form of the local gradient-elasticity balance of momentum. The displacement is thus the only unknown field. Zero generalized Neumann conditions are adopted along the top and bottom edges of the mesh and also along the contour of the *crack*.

Without using force measurements, the elastic constants are identified to a multiplicative factor. It is chosen to fix the C_{1111} coefficient to its initial value. The parameters related to $\underset{\approx}{\mathbf{C}}$ have an influence on the displacement field of a different nature than the parameters of $\underset{\approx\approx}{\mathbf{A}}$. Consequently, the minimization of Equation (15) is achieved using a fixed-point algorithm. While the second order parameters are fixed, the first order parameters are searched for by using a Newton algorithm. Then, we proceed in the complimentary way: the second order parameters are searched for

while the first order parameters are fixed. Concerning this second step of Newton search, the sensitivity of the cost function to minimize is significantly different from one parameter to another. To illustrate this point, an eigen value decomposition of the search direction is performed. We obtained the following normalized eigen values: $\{1, 0.017, 0.008, 0.0007, 0.0001\}$. In practice, this means that a single combination of the 5 second order elastic constants can be identified properly. Following Gras et al. (2013), a penalization of the Newton search is adopted. The initial cost function is supplemented by the quadratic gap between the actual parameters and the initial ones. The penalty factor is set to 100 compared to the average diagonal component of the search direction. The convergence criterion for the Newton search is written in term of the maximum of the parameters' increment over their initial guess. The stopping value is set to 10^{-4}. The fixed-point iterations are stopped once a stagnation of the cost function is obtained: if the reduction of the cost function relative to its initial value is smaller than 10^{-2}, convergence is considered. The set of initial parameters for both the first and the second order elastic tensors are obtained by second order periodic homogenization. The scheme adopted is as proposed in Kouznetsova et al. (2002). The initial elastic operators obtained using this scheme are:

$$\underset{\approx}{\mathbf{C}}_{ini} = \begin{bmatrix} 241 & 168 & 0 \\ 168 & 241 & 0 \\ 0 & 0 & 73 \end{bmatrix} \text{MPa} \tag{16}$$

and

$$\underset{\approx\approx}{\mathbf{A}}_{ini} = \begin{bmatrix} 29 & 0 & 0 & -29 & 14 & 0 \\ 0 & 112 & -20 & 0 & 0 & 20 \\ 0 & -20 & 24 & 0 & 0 & -25 \\ -29 & 0 & 0 & 29 & -15 & 0 \\ 14 & 0 & 0 & -15 & 116 & 0 \\ 0 & 20 & -25 & 0 & 0 & 25 \end{bmatrix} \text{MPa.mm}^2. \quad (17)$$

The initial values for the five intrinsic constants, $b_{11}, b_{22}, b_{33}, b_{13}$ and b_{35} are: 29, 24, 116, 15 and -21 MPa.mm^2 respectively.

4.3. Results

After convergence is reached, the elastic operators are

$$\underset{\approx}{\mathbf{C}}_{opt} = \begin{bmatrix} 241 & 151 & 0 \\ 151 & 241 & 0 \\ 0 & 0 & 90 \end{bmatrix} \text{MPa} \quad (18)$$

and

$$\underset{\approx\approx}{\mathbf{A}}_{opt} = \begin{bmatrix} 35 & 0 & 0 & -8 & 15 & 0 \\ 0 & 70 & -29 & 0 & 0 & 28 \\ 0 & -29 & 9 & 0 & 0 & 5 \\ -8 & 0 & 0 & 22 & -16 & 0 \\ 15 & 0 & 0 & -16 & 83 & 0 \\ 0 & 28 & 5 & 0 & 0 & 22 \end{bmatrix} \text{MPa.mm}^2. \quad (19)$$

The final values of the five intrinsic constants, $b_{11}, b_{22}, b_{33}, b_{13}$ and b_{35} are: 35, 22, 83, 15 and -22 MPa.mm^2 respectively.

To illustrate the reduction of the cost function, Figure 8 presents the norm of the gap between the measured displacement and those obtained by a numerical simulation with: the initial parameters, the parameters after the first Newton search on the first

order elastic parameters and the optimal parameters. The values of the cost function for these three cases are: 0.35, 0.16 and 0.12 pixel^2 respectively. The optimization of the first and the second elastic constants thus leads to a significant reduction of the *distance* between the measured and the simulated displacement. To further illustrate this reduction and to further validate the use of a gradient-elasticity model for describing the behaviour of the honeycomb material, the optimization is also run for the sole first order elasticity ($\underset{\approx\approx}{\mathbf{A}} \equiv 0$). The cost function value is then 0.17 pixel^2. This value being slightly higher than the value obtained for gradient-elasticity with the first order optimization and even higher than the value for gradient-elasticity with optimized elastic operators, the validity of gradient-elasticity is evidenced again.

The main modification of the first-order elastic parameter allows to describe more accurately the *Poisson*'s effect of the structure (its contraction due to the global tensile loading). A deeper insight in the differences between the displacement field highlights this suggestion: the major contribution to the gap between the experimental displacement and the numerical one, is obtained close to the top and the bottom edges in Figure 8(a) and it mainly affects the vertical component of the displacement. The changes in the second-order constants are more difficult to interpret. However, the major changes concern b_{11} and b_{33} which are closely related to κ_{111} and κ_{221}. The link between these to strain-gradient components is likely to consider as a second-order *Poisson*'s effect which was not predicted accurately, mainly due to the imperfection of the actual honeycomb geometry compared to the model used in effective properties estimation by homogenization.

The map of the remaining gap is difficult to interpret. Many reasons could be invoked to explain the distribution of the distance between the experimental displacement and the solution of the gradient-elasticity simulation with optimized parameters. One of the first reasons should be the non-linear response of the constitutive material

used to print the specimen. Uniaxial tensile tests were performed and a non-linear response was observed from 2% strain. Whereas longitudinal strain in Figure 6 is below 2% except in the vicinity of the *crack*. Higher strain level is most probably experienced by the material locally at the cell corners. The far distance influence of this localized phenomena may take the shape of the red to green area in Figure 8(c). To reduce the potential effect of these non-linearites, the analysis was repeated for a deformed image g acquired for a lower load level. No significant difference was obtained neither on the shape of the residual map nor on the values of the identified parameters. Another explanation for this remaining gap is that gradient-elasticiy is not rich enougth for capturing the behaviour of the honeycomb at the *crack* vicinity. This deficiency may also have a long distance influence due to structural effects induced by the presence of the *crack*. Another point is the *crack* geometry. In the analyses presented herein, it has been considered as a notch which shape and dimension match exactly the hole formed by the removed cells. The effective shape of the *crack*, in the gradient-elasticity context, is more likely different from the actual one. This might also induce modifications of the displacement field around the *crack*. Yet the geometry of the *crack* is uncertain, further, the boundary conditions to applied along its faces in the context of gradient-elasticity is an even more complex question. Zero generalized Neumann conditions have been adopted without further validation. This should also induce discrepancy over the zone surrounding the *crack*.

5. Conclusion

Based on an experiment performed on a sample with a honeycomb structure and a *crack*, the investigation of gradient-elasticity at the macroscopic scale and the identification of the constitutive model parameters are carried out. The validation of the second order continuum is achieved through the analysis of the displacement field

measured by digital image correlation at two different scales. The displacement is indeed estimated at the macroscopic scale but also at the microscopic scale around each individual cell of the honeycomb. The displacement field along the cells' boundary is post-processed in order to extract the meaningful parameters for the purpose of validation and comparision with the macroscopic field. The used of gradient-elasticity at the macroscopic scale is justified in two steps: first it is shown that a second order kinematic is required to capture the deformation of the unit cells; then, the micro-morphic displacement gradient is found to match the macroscopic strain. The usual kinematic relations between the micro-scale displacement and the macroscopic one are thus validated. From the analysis of the additional fluctuation of the displacement along the cells' boundary and its periodicity, it is concluded that gradient-elasticity is appropriate to account for micro-struture effects at the macroscopic level.

After the kinematic of the continuum model has been defined and validated, the material constants are identified by using a model updating procedure. Through the minimization of the distance between the experimental displacement and the one obtained by gradient-elasticity numerical simulations, optimal first and second order elastic operators are obtained. A significant reduction of the cost function is achieved through the use of gradient-elasticity compared to the first-order elasticity. While several open questions still remain, concerning *e*.g. the effective shape of the *crack* to consider within the context of gradient-elasticity or the effectiveness of zero traction and zero double-traction assumptions along the *crack*, the proposed methodology leads to the validation of a strain-based micro-morphic elastic model and the identification of the full set of its related material constants from experimental data.

Acknowledgements

The support of Pays de la Loire, through grant MatSyMat, labelled by EMC2, is gratefully acknowledged.

References

Auffray, N., Bouchet, R., Brechet, Y., 2009. Derivation of anisotropic matrix for bi-dimensional strain-gradient elasticity behavior. International Journal of Solids and Structures 46 (2), 440–454.

Besnard, G., Hild, F., Roux, S., 2006. 'finite-element' displacement fields analysis from digital images: Application to portevin-le châtelier bands. Experimental Mechanics 46 (6), 789–803.

Boutin, C., 1996. Microstructural effects in elastic composites. International Journal of Solids and Structures 33 (7), 1023–1051.

Burteau, A., N'Guyen, F., Bartout, J.-D., Forest, S., Bienvenu, Y., Saberi, S., Naumann, D., 2012. Impact of material processing and deformation on cell morphology and mechanical behavior of polyurethane and nickel foams. International Journal of Solids and Structures 49 (19), 2714–2732.

Cosserat, E., Cosserat, F., Brocato, M., Chatzis, K., 1909. Théorie des corps déformables. A. Hermann Paris.

Dasgupta, S., Sengupta, D., 1990. A higher-order triangular plate bending element revisited. International Journal for Numerical Methods in Engineering 30 (3), 419–430.

Eringen, A., Suhubi, E., 1964. Nonlinear theory of simple micro-elastic solids-i. International Journal of Engineering Science 2 (2), 189–203.

Forest, S., 1998. Mechanics of generalized continua: construction by homogenizaton. Le Journal de Physique IV 8 (PR4), Pr4–39.

Forest, S., Trinh, D. K., 2011. Generalized continua and non-homogeneous boundary conditions in homogenisation methods. ZAMM-Journal of Applied Mathematics and Mechanics/Zeitschrift für Angewandte Mathematik und Mechanik 91 (2), 90–109.

Gologanu, M., Leblond, J., Perrin, G., Devaux, J., Suquet, P., 1995. Continuum micromechanics. Berlin: Springerverlag, 61.

Gras, R., Leclerc, H., Roux, S., Otin, S., Schneider, J., Périé, J.-N., 2013. Identification of the out-of-plane shear modulus of a 3d woven composite. Experimental Mechanics 53 (5), 719–730.

Kavanagh, K., Clough, R., 1971. Finite element applications in the characterization of elastic solids. International Journal of Solids and Structures 7, 11–23.

Kouznetsova, V., Geers, M., Brekelmans, W., 2002. Multi-scale constitutive modelling of heterogeneous materials with a gradient-enhanced computational homogenization scheme. International Journal for Numerical Methods in Engineering 54 (8), 1235–1260.

Leclerc, H., Perie, J., Roux, S., Hild, F., 2009. Computer Vision/Computer Graphics CollaborationTechniques. Springer, Berlin, Ch. Integrated Digital Image Correlation for the Identification of Mechanical Properties.

Mindlin, R., 1964. Micro-structure in linear elasticity. Archive for Rational Mechanics and Analysis 16 (1), 51–78.

Réthoré, J., 2010. A fully integrated noise robust strategy for the identification of constitutive laws from digital images. International Journal for Numerical Methods in Engineering 84, 631–660.

Réthoré, J., Hild, F., Roux, S., 2008. Extended digital image correlation with crack shape optimization. International Journal for Numerical Methods in Engineering 73 (2), 248–272.

Réthoré, J., Muhibullah, Elguedj, T., Coret, M., Chaudet, P., Combescure, A., 2013. Robust identification of elasto-plastic constitutive law parameters from digital images using 3d kinematics. International Journal of Solids and Structures 50 (1), 73–85.

Toupin, R., 1964. Theories of elasticity with couple-stress. Archive for Rational Mechanics and Analysis 17 (2), 85–112.

Figures

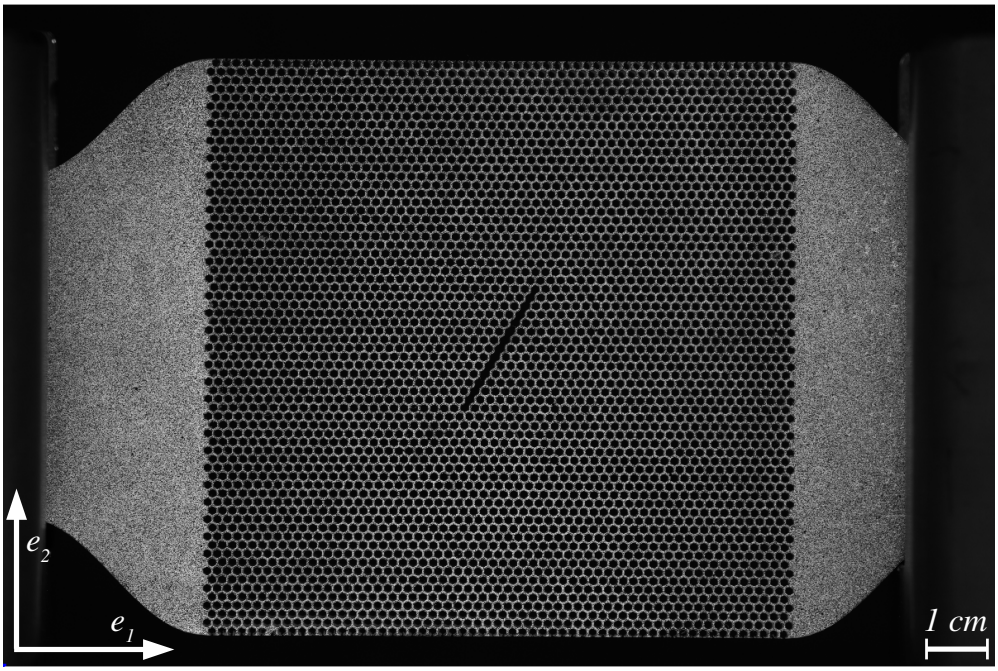

Figure 1: Image of the sample in the tensile device. The image has a definition of 6576×4384 pixels.

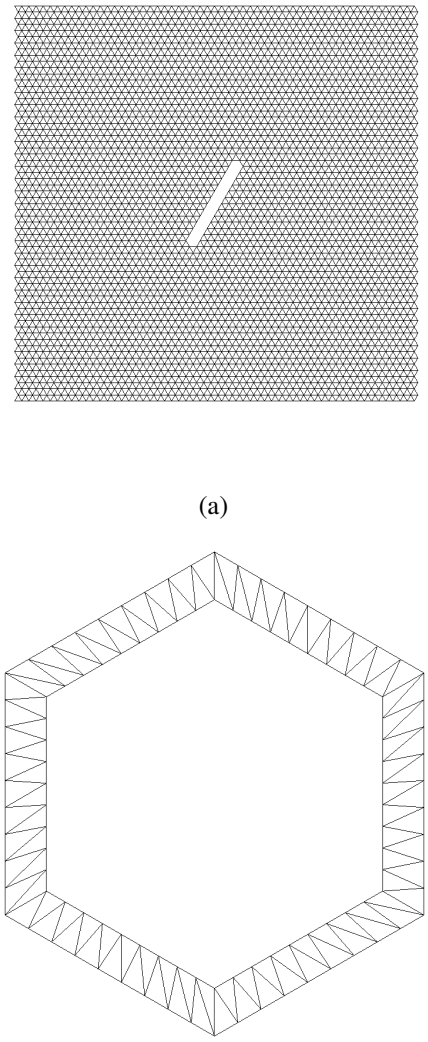

(a)

(b)

Figure 2: Finite element meshes used to perform DIC analyses. (a) finite element mesh for macroscopic scale, (b) mesh of a unit cell.

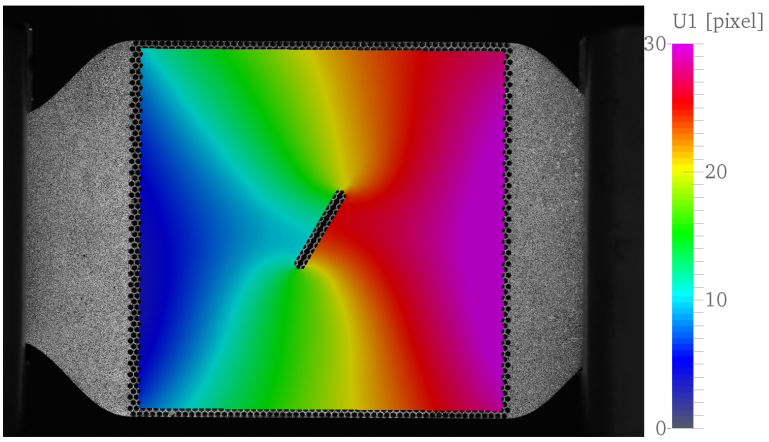

(a)

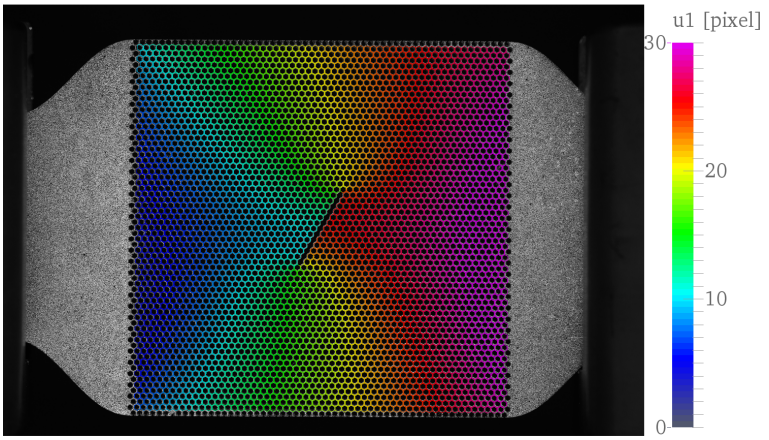

(b)

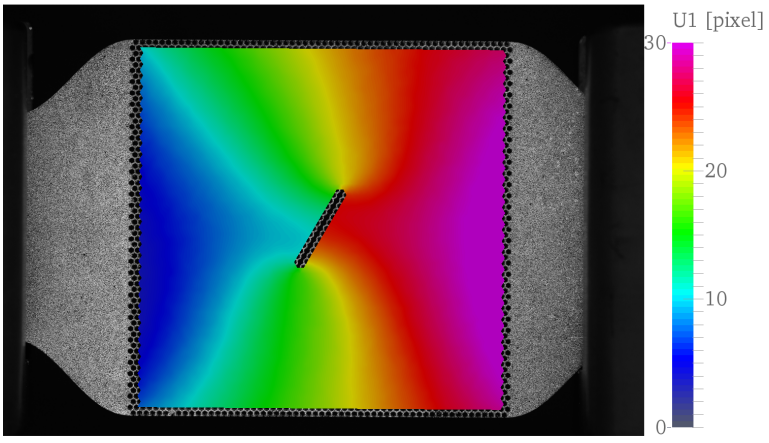

(c)

Figure 3: Horizontal displacement field in pixel for: (a) the macroscopic analysis $\underline{\mathbf{U}}$, (b) the analysis of the microscopic displacement $\underline{\mathbf{u}}$ and (c) the mean value of the microscopic displacement $\underline{\mathbf{u}}$ for each cell.

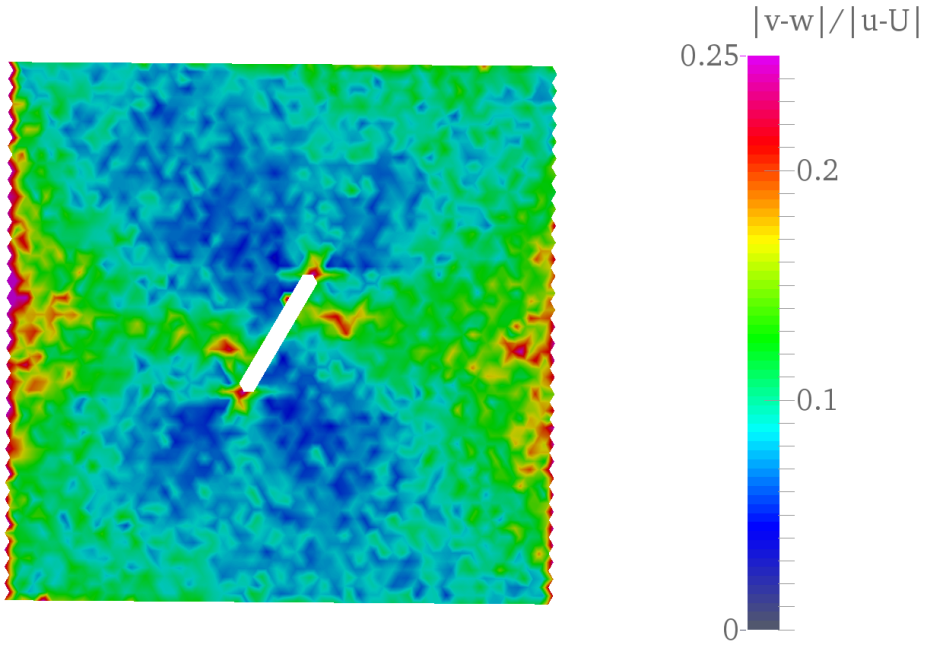

(a)

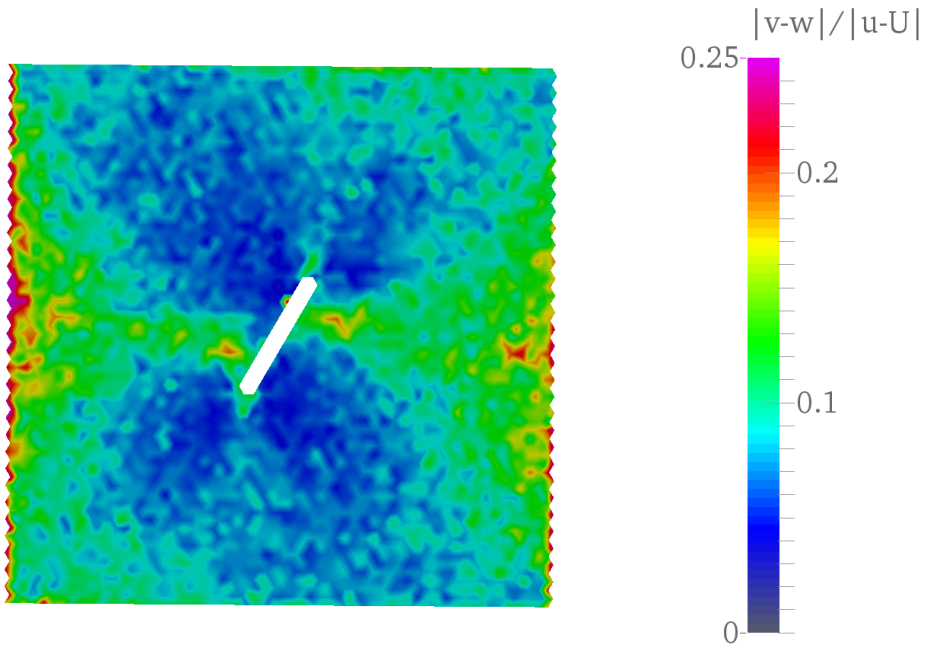

(b)

Figure 4: Norm of the non-periodic part of projection residual $\underline{\mathbf{v}} - \underline{\mathbf{w}}$ of the effective boundary displacement of the unit cells normalized with respect to the norm of the effective displacement $\underline{\mathbf{u}} - \underline{\mathbf{U}}$ for: (a) a first order polynomial, (b) a second order polynomial as defined in Equation (4).

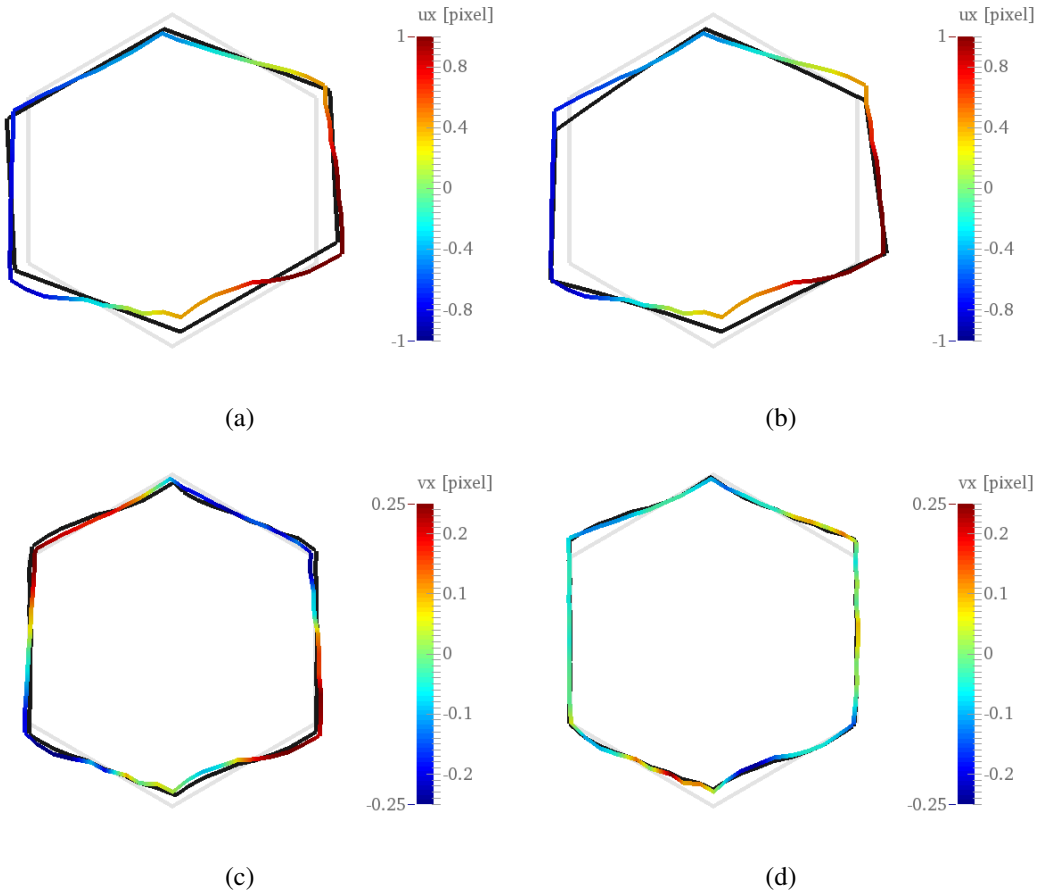

Figure 5: Analysis of boundary kinematics of the unit cell at the crack tip. On the top, the actual deformation of the unit cell by the effective displacement $\underline{\mathbf{u}} - \underline{\mathbf{U}}$ is plotted together with its projection on a linear (left), quadratic (right) polynomial (in black). On the bottom, the projection residual $\underline{\mathbf{v}}$ is plotted with its periodic part $\underline{\mathbf{w}}$ (in black). The deformation of the unit cell boundary have been amplified 5 times.

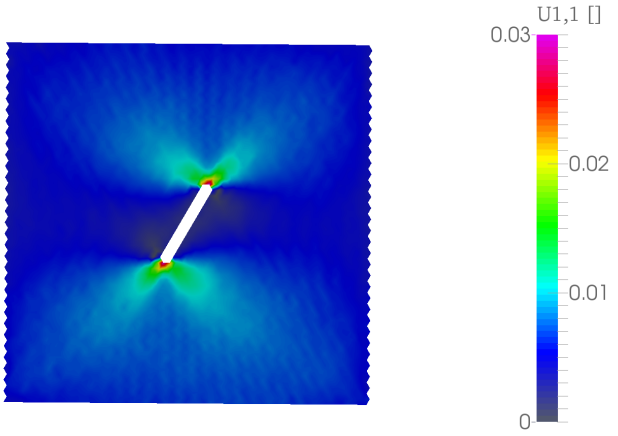

(a)

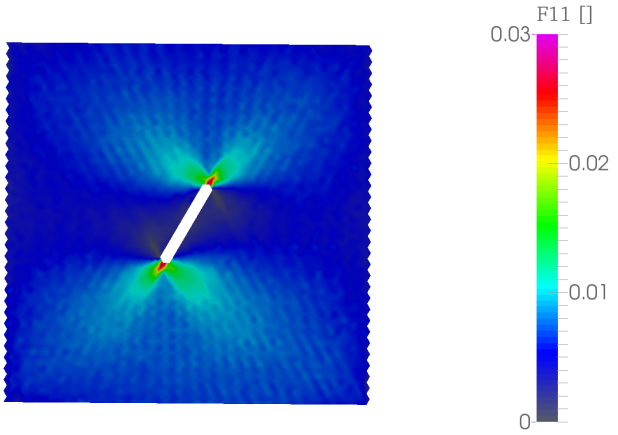

(b)

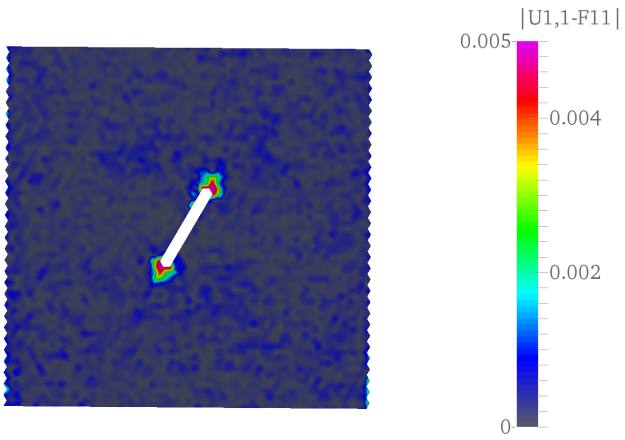

(c)

Figure 6: Component $_{11}$ of : (a) the macroscopic displacement gradient $U_{1,1}$, (b) the micro-morphic tensor F_{11} and (c) the relative strain $U_{1,1} - F_{11}$.

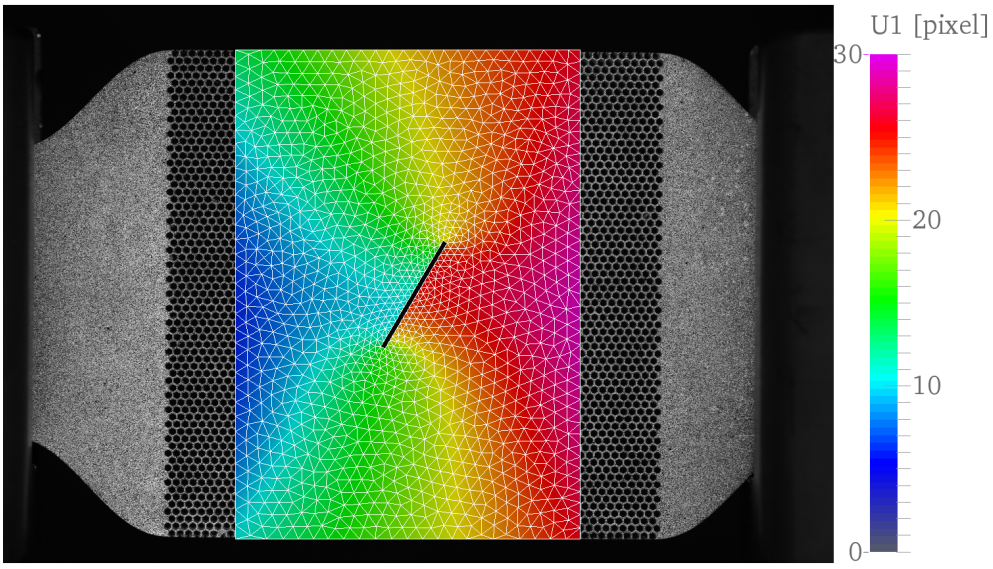

Figure 7: Horizontal displacement field in pixel obtained with the mesh used for the identification of the material constants.

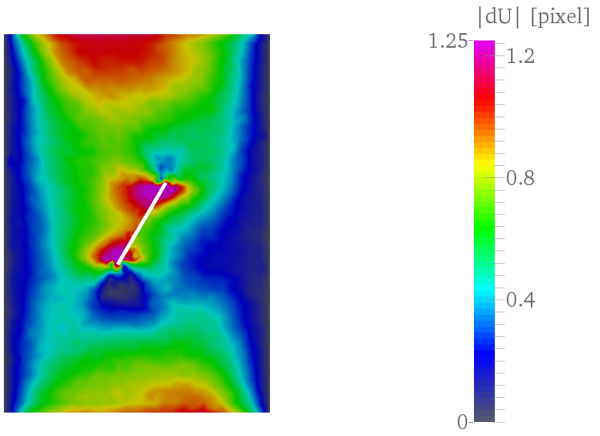

(a)

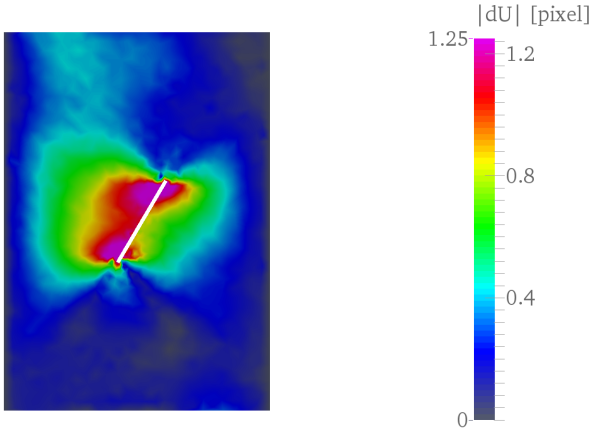

(b)

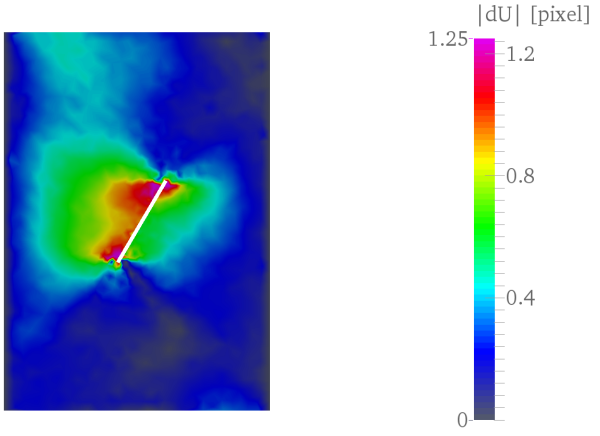

(c)

Figure 8: Norm of the gap between the measured displacement and those obtained by a numerical simulation with: (a) the initial parameters, (b) the parameters after the first Newton search on the first order elastic parameters and (c) the optimal parameters.